The Effects of Debulking on the Microstructure of Carbon Fiber Reinforced Composites

MATHEW SCHEY, SCOTT STAPLETON and TIBOR BEKE

ABSTRACT

Carbon fiber reinforced plastics (CFRPs) are widely used due to their high strength to weight ratios. A common process manufacturers use to increase the strength to weight ratio is debulking. Debulking is the process of transversely compacting a dry fibrous reinforcement prior to wet out with the matrix resin, in order to induce fiber nesting, effectively increasing the volume fraction of the sample. While this process is widely understood macroscopically its effects on fibrous microstructures have not yet been well characterized.

The aim of this work is to compare the microstructures of three CFRPs, varying only the debulking step in the manufacturing process. The microstructural effects of debulking on three unidirectional CFRPs made from three different levels of debulking were studied. High resolution serial sections of all three samples were taken using the UES ROBO-MET at the NASA Glenn Research Center in Cleveland, Ohio. Using these scans, the fiber positions were measured and connected to make fiber paths. Statistical descriptors such as local fiber and void volume fractions, and void distribution and morphology were then generated for each sample and compared. Using these descriptors, the effects of debulking on the composite microstructure can be measured.

Mathew Schey, Scott Stapleton, Tibor Beke, University of Massachusetts Lowell, 220 Pawtucket Street, Lowell, Massachusetts 01854, U.S.A.

INTRODUCTION

Carbon fiber reinforced plastics (CFRPs) are widely used as a high-performance material due to their high strength to weight ratios. Traditionally, such CFRP's are manufactured with a carbon fiber textile reinforcement, pre-impregnated with the matrix resin (i.e., "prepreg"). To reduce costs, the industry has been moving towards molding with dry reinforcements using a family of processes known as liquid composite molding (LCM). Compared to prepreg materials, working with dry reinforcements incurs fewer material costs, less material waste from both trim and expiration, less freezer storage energy, and more flexibility with complex part geometries. In LCM, the dry reinforcement is laid on the tool, and the fibers are subsequently wet out with the resin, either by over-pressure in resin transfer molding (RTM) or vacuum draw in vacuum infusion (VI). VI is more economically suited to larger parts as the mold consists of one-sided tooling, only rigid enough to support vacuum pressure, and a vacuum bag covering the other side of the reinforcement [1] [Williams].

Due to the use of a flexible vacuum bag, the driving force for the resin wet-out in VI is limited to vacuum pressure only, whereas wet-out in RTM may be performed at whatever pressure the equipment is capable of. This greatly limits the flow velocity, especially for a large part as viscous shear of the fibers slows down the flow velocity as the flow front travels further from the inlet. The ability to consolidate the CFRP is limited as vacuum pressure by itself cannot squeeze out as much excess resin, compared to applying over-pressure to the bag in an autoclave cure, or the high pressures usually involved in RTM. This in turn limits the achievable fiber volume content which is directly tied to the part's mechanical performance. The lower pressures involved in VI also usually result in higher void content. Any such bubbles trapped in the part after resin cure are then known as voids and act as a further detriment to mechanical performance [2–7]. In comparison with prepreg, all forms of LCM processing also suffer from a less homogeneous distribution of such voids due to the in-plane pressure gradient applied during resin wet-out [8–10]

A common process manufacturers use to mitigate the problems of the thickness gradient and low fiber content in VI is debulking. Debulking is the process of transversely compacting a dry fibrous reinforcement prior to wet out with the matrix resin, in order to induce fiber nesting. A hysteresis is seen through repetition of the compaction, where the reinforcement moves to a more nested and compressed state [11–16]. Upon VI processing of such a debulked reinforcement, the same vacuum application and ambient pressure will result in a higher fiber volume fraction than without the debulking [16]. In addition, a debulked reinforcement exhibits less compliance, and thus less of a thickness gradient along the resin flow path [16].

The literature on debulking has focused on experimental determination of the changes in required displacement to reach a target pressure, or vice-versa, while iterating parameters such as compaction rate, ply count, and reinforcement material [11–16]. Such studies have shown that e.g. 1) higher rate causes less compliance [13, 14], 2) varying the ply count causes a significant difference in compressibility for only very low ply counts [15], and 3) the increase in nesting between cycles decreases with each subsequent cycle [11, 12, 14, 16, 17]. Some reinforcement compaction studies have focused on the compressibility of the reinforcement during vacuum infusion processing [18–20], again without examining the effects of pre-infusion debulking.

While the micro-structural mechanisms of reinforcement compaction have thus been studied for low cycle counts, only more empirical results have been presented for true debulking practice. The effects of debulking on fibrous microstructures have not yet been well characterized. The one known study on this subject showed a lateral spreading of the fiber tows during the first compaction cycle, leading to a significant rise in the maximum fiber content, and a dependence on the frictional characteristics of the fiber contacts for further cycles beyond the first [12]. This difference in mechanisms between the first compaction and later ones suggests that the models developed for the compaction occurring during VI processing, based on no debulking [20], cannot accurately predict similar behavior for a debulked reinforcement. Industrial debulking practice is typically developed in a trial-and-error process by individual companies or even individual operators. This study aims to investigate the actual microstructural mechanism that leads to increased compaction during debulking, to enable a better understanding of what process parameters lead to the fastest and most effective debulking practice.

During LCM processing including VI, small amounts of gas are mechanically trapped as bubbles due to the dual scale flow including flow between the fiber tows, and flow within the fiber tows [21, 22]. The trapped gas comes from either the resin itself, or from lingering atmospheric gas amid the fibers. Inter-tow macro-voids are formed when the flow front velocity is low and the intra-tow capillary flow outpaces the inter-tow bulk flow [21]. Intra-tow micro-voids may be formed in the opposite case when the flow front velocity is high and outpaces capillary flow [23, 24].

Although debulking may result in enhanced mechanics, it comes at a cost of processability. Greater debulking causes an increase in the fiber volume content, and thus slower filling velocities. As per the dual scale void formation theory outlined above, this should result in more formation of macro-bubbles, i.e. those formed between the tows. With the tighter fiber packing, this will also result in more fiber shear, and less ability for the trapped bubbles to be flushed to the flow front and out of the resin [25], thus further exacerbating the final void content. No previous studies have investigated this trade-off, namely, how much of an increase in filling time and void content result from a particular amount of debulking.

The aim of this work is to compare the microstructures of three CFRPs, varying only the debulking step in the manufacturing process. The microstructural effects of debulking on three unidirectional CFRPs made from three different levels of debulking were studied. High resolution serial sections of all three samples were taken using the UES ROBO-MET at the NASA Glenn Research Center in Cleveland, Ohio. Using these scans, the fiber positions were measured and connected to make fiber paths. Statistical descriptors such as local fiber and void volume fractions, and void distribution and morphology, were then generated for each sample and compared. Using these descriptors, the effects of debulking on the composite microstructure can be measured.

METHOD

Three stacks of carbon fiber plies were subjected to three different levels of debulking before infusion. During the debulking procedure various measurements were made and recorded. Once infused and cured, samples were taken from all three laminates and prepped for imaging. The samples were imaged using an automated

serial sectioning machine. After imaging the scans were analyzed and both fiber paths and voids were extracted. Metrics for both the fibers and voids were then generated.

Materials

The fibers used in each composite plate were 24K fiber/tow unidirectional plies. The resin used was RIMR-135 resin with RIMH 1366 curing agent.

Experimental Procedures

Debulking steps were applied to three stacks of carbon fiber reinforcement plies. These samples were then infused, and the infused samples were then imaged and fiber paths were extracted, as well as voids.

DEBULKING AND COMPRESSIBILITY TESTING

Various amounts of debulking were performed by compressing the reinforcement samples in a universal testing machine (UTM), at different cycle counts, displacement rates and durations of compression ("dwell times"). Three samples of reinforcement were used in conducting these experiments: "sample-1"- a low debulk sample, "sample-2"- a high-debulk sample, and "control"- sample. All three of these samples were comprised of four plies, each cut to 25.4 mm x 25.4 mm, of a dry, carbon-fiber, unidirectional weave reinforcement.

Three different methods of debulking cycles were performed:

- 1) "Method A" consisting of fast displacement rates and no dwell time. These tests consisted of a fast oscillating pressure application, applying 100 kPa, then no dwell time, i.e. immediately relaxing the sample to no compression. The entire oscillation cycle lasted two to four seconds.
- 2) "Method B" consisting of medium displacement rates and medium dwell time. Displacement was performed at a constant applied $\Delta P/\Delta t$ (P and t are pressure and time, respectively) equal to 3.5 kPa/s for both compression and relaxation. The machine converted to constant force-hold once reaching 100 kPa and held that pressure for a five-minute dwell time, by continual slight compression of the sample to counteract the creep deformation caused by fiber rearrangement (i.e. nesting). One cycle lasted about six minutes.
- 3) "Method C" consisting of slow displacement rates and long dwell time. This method simulates the vacuum infusion process at the ambient pressures at Utah mountain elevation, where the laminates were later infused. The sample was first compressed at 4 mm/minute, until reaching a pressure of 86 kPa, then holding that pressure for a dwell time of 15 minutes, then releasing the pressure at approximately 0.04 mm/minute. The 15-minute dwell time mimics the preparation time before starting the infusion, and the slow relaxation rate mimics the slow expansion of the fibers as the resin wets out the preform and develops a fluid pressure under the vacuum bag.

The sequence of debulking for each of the three samples is summarized in Table 1. The control sample went through three successive cycles of Method C debulking.

Samples 1 and 2 also did the same three cycles of Method C debulking, but were subjected to additional cycles of Method A and B, sometimes separated by a time delay in days.

TABLE I - DEBULKING TEST SUMMARY

Sample	Step 1	Step 2	Step 3	Step 4	Step 5	Step 6	Step 7	Step 8
Control	3 x C	-	-	-	-	-	-	-
1	60 x A	2 days	1 x C	6 days	1 x C	5 x B	1 day	1 x C
2	240 x A	2 days	1 x C	6 days	1 x C	10 x B	1 day	1 x C

In each debulk test, both force (F) and extension (ϵ) were recorded at a frequency of 10 Hz. The force data was converted to pressure (P) by dividing the force by the sample-area under compression. The extension data was corrected for machine flex by first ascertaining the extension required by the UTM machine itself, with no fabric sample, to reach the hold-pressure. Using theory of parallel springs, all sample thickness data was then corrected by subtracting the system extension at a given force from the UTM-recorded extension at the same force. The corrected extension data was then converted to sample thickness (h), which was in turn converted to fiber volume content v_F using the formula:

$$v_F = \frac{nA_W}{h\rho_F} \tag{1}$$

where n, A_W , and ρ_F represent the number of plies, reinforcement areal weight, and fiber density, respectively. The carbon reinforcement used in this study has an areal weight of 756 g/m² and fiber density of 1770 kg/m³.

Figures 1, 2, and 3 show example graphs of the recorded sample thickness *h* during the pressure oscillation, respectively for Method A, B, and C debulking.

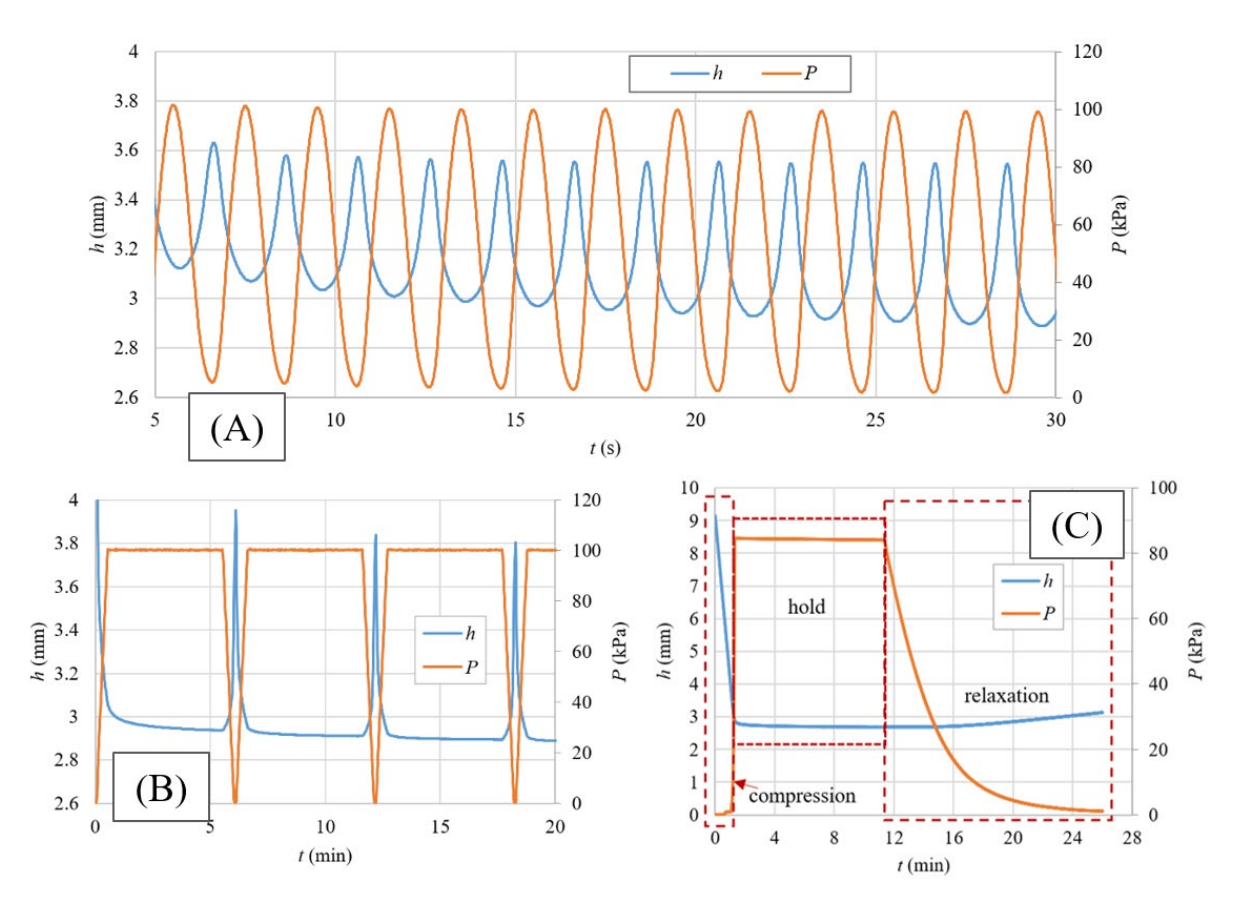


Figure 1. Method A (top), Method B (bottom left), and Method C (bottom right: pressure and ample thickness oscillation

VACUUM INFUSION PROCESS

Three samples were infused by vacuum infusion under a vacuum bag, using a layer of flow media over the top to accelerate the filling time. Two of the samples were the same samples 1 and 2 from the debulking experiments, which were infused shortly after the last method C cycle. Samples 1 and 2 will be referred to here on as the "low" and "high" debulk samples, respectively. The third preform was a fresh sample straight from the fabric roll, with no debulking, cut to the same ply count and dimensions as the low and high debulk samples.

An inlet channel was situated across one of the edges of the sample to create approximately uni-directional flow across the square preform. Flow media covered all the surface of the preform except for an approximately 20 mm wide perimeter along the vent-side of the preform as well as the sides perpendicular to the flow direction. An epoxy system, RIM-R 135 and RIM-H 1366, was used for the infusions. The resin was mixed, then degassed for 15 minutes before infusion. The applied pressure gradient was 86 kPa.

The resin viscosity was measured just prior to infusion with a Brookfield viscometer, and was approximately 360 mPa·s for all three infusions. Thermocouples verified that the epoxy resin, both in the pot and in the mold, remained at nearly a constant temperature, approximately 21° C.

After filling the preform, the inlet pipe from the resin pot was clamped shut and the preform left under vacuum until the part was cured. Upon demolding, some dry areas were noticed on the rigid mold-side of sample-2 (Figure 2). This denotes the tortuous path of the resin from the flow media through the thickness of a uni-directional weave, with relatively low permeability compared to other reinforcements, and exacerbated by the high debulking.

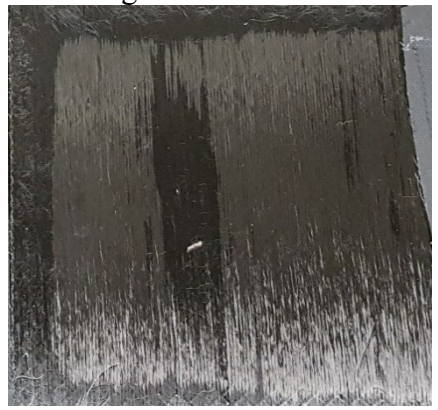


Figure 2. Dry fibers on back side of sample 2

SAMPLE PREP AND IMAGING

Rectangular samples were taken from each carbon fiber plate, each of which were 3mm x 20 mm x 50 mm in size. Once the samples were cut out they had to be sanded in order to remove the layer of peel ply on each of them. Care was taken to make sure the sanding operation on each sample was as consistent as possible. This was done to ensure the samples were all of similar thickness, and to make sure each individual had as uniform thickness as possible.

Serial sections were taken using the UES Robo-Met.3D machine at the NASA Glenn Research Center in Cleveland, Ohio. Due to fiscal and time constraints associated with the automated serial section process it was decided that all three samples would be stacked on top of each other and scanned at once. Samples were then clipped together and potted in resin.

Once the potting resin cured the new unified sample was placed in the Robo-Met's "kinematic sample holder", a jig which clamps on to the sample and provides grips for the robotic arm to grab on to. The sample and holder were then placed on the alignment jig, which allowed the sample to hover above the microscope.

The serial sectioning process starts with a polishing step, in which a particulate solution is squirted on to a textured circular plate. Once rotating this plate acts like sand paper, but offers more precision in terms of material removed and the resulting quality of the surface. A number of polishing steps were performed before each new image was taken of the sample. Each polishing step contained smaller particulate matter than the previous, which mimicked the use of higher grit sand paper in typical sanding operations. All of the steps contained two preparation steps in which the sample was rinsed and air dried, except for step 4 which had an additional ultrasonic bath step. After all polishing steps the kinematic sample holder was returned to the alignment jig for imaging.

Images for each layer were taken in sections and stitched together later. The alignment jig started in one corner of the sample (the upper left corner of the final image) and moved in columns until it had captured all of the locations specified for the sample. After each set of images were taken for each layer they were stitched together

to make a mosaic. This process was done automatically using the accompanying software for the Robo-Met machine. The total time to completion was 12.5 days. The final resolution for each image came out to be $0.51~\mu\text{m/px}$ in the yz plane, and an average of $2.5~\mu\text{m/px}$ in the scan direction. Due to the difficulty of removing a consistent amount of material each polishing step, the distance between successive scans varied. For the purpose of this analysis the average value of $2.5~\mu\text{m/px}$ was used.

TABLE II. BREAKDOWN OF ROBO-MET RECIPE

				Sweep Speed	Rotation Speed
Step	Pad/Cloth	Solution	Time (Sec)	(Deg/Sec)	(Deg/Sec)
1	Largo	6 μm Diamond	180	60	30
2	DAC	3 μm Diamond	180	60	30
3	DAC	1 μm Diamond	180	60	30
4	MD-Chem	Colloidal Silica	180	60	30

IMAGE ANALYSIS

Three factors added to the complexity of image analysis. The image frames corresponding to successive layers were imperfectly aligned, which we contribute to inaccuracies in the motion of the kinematic sample holder. These degree of misalignment between frames was well over the size of a fiber diameter. As the optical microscope scanned the specimen, uneven lighting created intensity variations within the 64 square-shaped sub-images that formed the total mosaic image. Finally, the optical images of many layers were marred by what appear to be films of liquid, presumably left over from the cleaning step of the polishing process. The frame misalignments were corrected with the help of ImageJ image stabilization software (Figure 3). The cells that made up each mosaic were also observed to be slightly out of alignment from one another. The magnitude of this variability, however, was not enough to significantly affect the results of fiber detection. The disk and void detection algorithms, described below, were able to handle the local intensity changes due to uneven lighting but the correction of irregular hue variations due to liquid spills proved challenging.

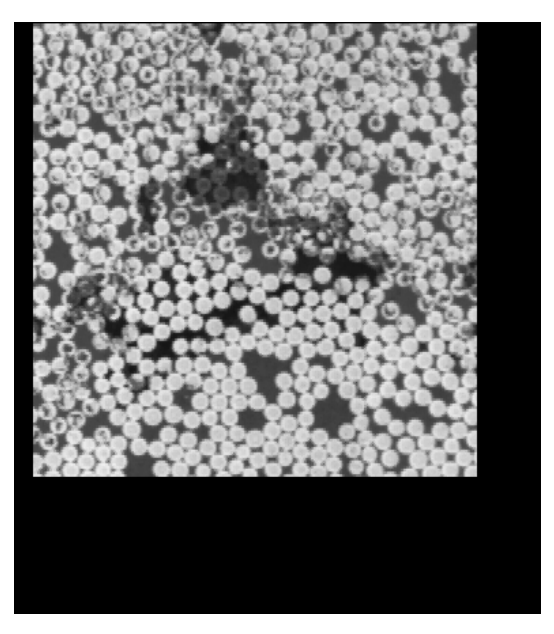


Figure 3. Subsection of the high debulk sample used to test the image registration program. The size of the surrounding black space represents the magnitude of the deviation in position from one frame to another

The fiber cross-sections in the image foreground consist of disks with soft, often partially overlapping boundaries, possibly occluded by dust particles or optical artifacts. The intensity of the fiber cross-sections exhibits a slight increasing gradient toward the center. The overlapping disk boundaries prevent the effective application of traditional edge detection as well as feature-based disk recognition algorithms like the Hough transform.

The initial method for fiber detection involved analyzing binarized versions of the cross-sectional images. The images were first read into a 3D array in MATLAB in which each page of the array represented one section. Each image was then converted to binary such the majority of the fibers appeared as white and the surrounding resin appeared as black. The MATLAB function "regionprops" was then used to find the centroids of all the disconnected white regions (mostly fibers) in the space. One of the major issues with this method was its inability to deal with the discoloration mentioned above (Figure 4).

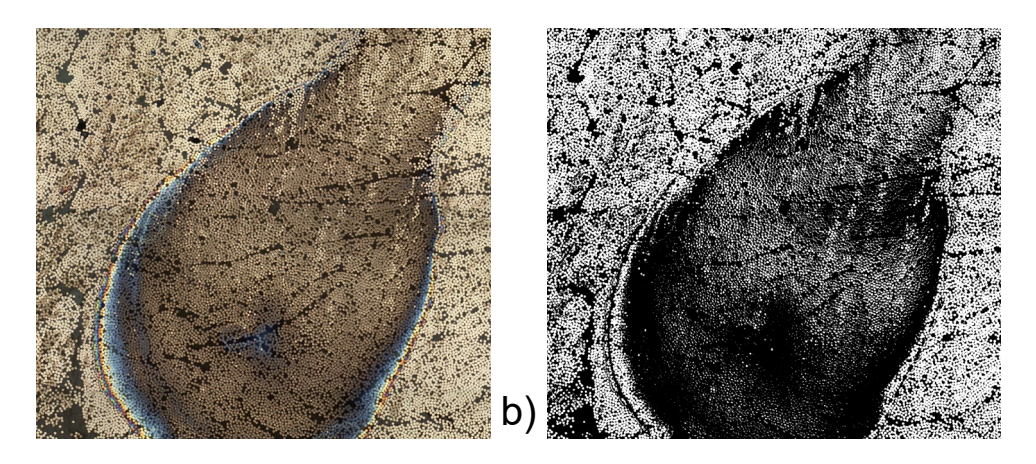


Figure 4. Example of the effects of discoloration on images a) before binarization and b) after binarization.

The major effect of these regions was that hundreds to thousands of fibers were masked in particular cross-sections, leading to large gaps in the resulting fiber path data. These regions were random in terms of both shape and frequency of appearance, making them more difficult to predict and correct.

To correct for these regions a number of image processing steps were added to the analysis method previously described. Prior to binarization the images were converted from RGB to grayscale using the open-source software ImageJ. This was followed by a morphological erosion operation in MATLAB, with a disk structuring element of radius one half of the average fiber radius (3 pixels or 1.51 μ m). Then, each image was subjected to a thresholding step, in which pixels with a grayscale intensity of 60 or less (on the standard 0-255 grayscale) to zero, leaving the rest of the pixels unaffected. After that, Gaussian smoothing was applied, with a Gaussian kernel of radius equal to the average fiber radius. This replaces each convex disk by a locally convex function with a unique maximum. To detect the fiber centers, the MATLAB function "imregionalmax" was used in conjunction with the function "regionprops". The function "imregionalmax" takes in an M x N grayscale image and outputs an M x N binary image showing white pixels at the locations of the regional maxima. These regional maxima corresponded to the centers or near-center locations within each fiber cross-section. The function "regionprops" was then used to find the exact pixel locations of these maxima as well as their area. It was discovered that a number of the regional maxima were not actually fibers but actually small image artifacts, often adjacent to one another. Many of these regions were removed by removing all the regions with an area greater than three. The cut-off value of three for area was found by doing trial and error until the best result was achieved. The entire process for a discolored region is shown in Figure 5.

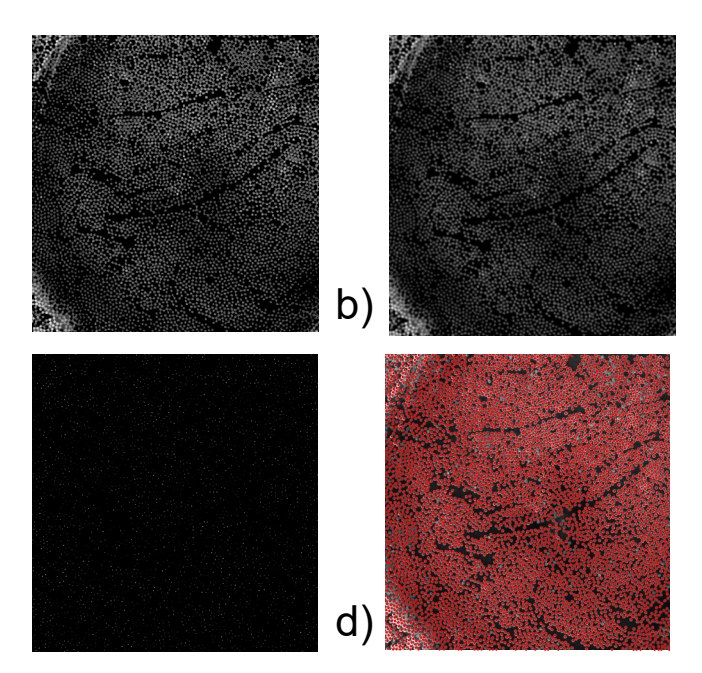


Figure 5. Entire image processing method showing a) eroded greyscale image after thresholding, b) image with Gaussian filter, c regional maxima, and d) resulting fibers detected

After the fiber center points were found in each cross-section, the center points had to be linked between cross-sections to form the fibers. Due to the stiffness of the fibers

and the relatively short spacing between images (compared with the fiber diameter), the fiber positions did not vary significantly between sequential cross-sections This permitted the use of a nearest-neighbor search algorithm from one cross-section to the next to link fibers. The process for detecting and filtering fibers is documented in full in [26].

In each sample, fiber paths were extracted from both individual tows and regions independent of tow positions (Figure 6). The purpose of this distinction was to compare metrics of fibers within tows to sample fibers representative of the layer as a whole. One of the downsides of the samples was the presence of blurry regions in the mosaic of images due to out of focus sections. These sections made the collection of global fibers difficult and led to significant overlap between the tows and the global regions. Furthermore, the location of stitch fibers in the low debulk layer made it difficult to take one global region. To solve this the region was split in half and placed in two different locations.

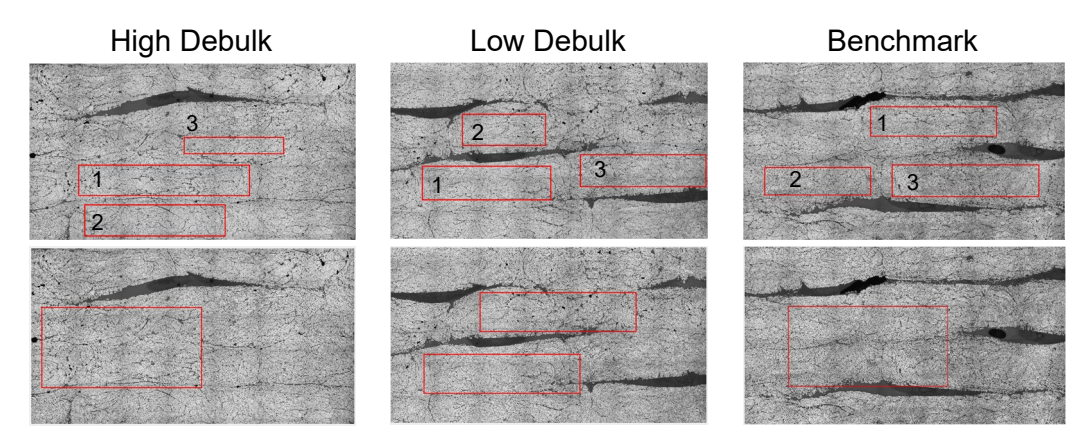


Figure 6. Cross-sections of the three samples imaged showing the analyzed tows (top) and global samples (bottom)

The size of the global samples were each 0.510 mm x 1.02 mm in area. The sizes of the intra-tow specimens varied and are listed in Table 3.

Layer	Tow 1 Dimensions	Tow 2 Dimensions	Tow 3 Dimensions	
	(mm)	(mm)	(mm)	
High	0.386 x 2.16	0.395 x 1.77	0.208 x 1.26	
Low	0.438 x 1.67	0.404 x 1.08	0.416 x 1.63	
Benchmark	0.377 x 1.61	0.352 x 1.35	0.407 x 1.88	

Table 1. Dimensions of the intra-tow fiber regions analyzed in each layer

Metrics

Spatial fiber metrics were measured from the extracted fiber paths. Additionally clusters were detected from the extracted fibers and metrics on the shape and size of the clusters were calculated.

LOCAL VOLUME FRACTION

The local volume fraction, v_f^i is the ratio of a fiber's cross-sectional area to the area of that fiber's Voronoi cell in a cross-section (Figure 7). Unlike the global volume

fraction, the local metric provides information on localized regions of high density or sparsity within the sample.

$$v_f^i(x_n) = \frac{\pi R^2}{A_v^i(x_n)} \tag{1}$$

where R is the radius of the fiber and $A_v^i(x_n)$ is the area of the Voronoi cell of fiber i at the cross-section x_n .

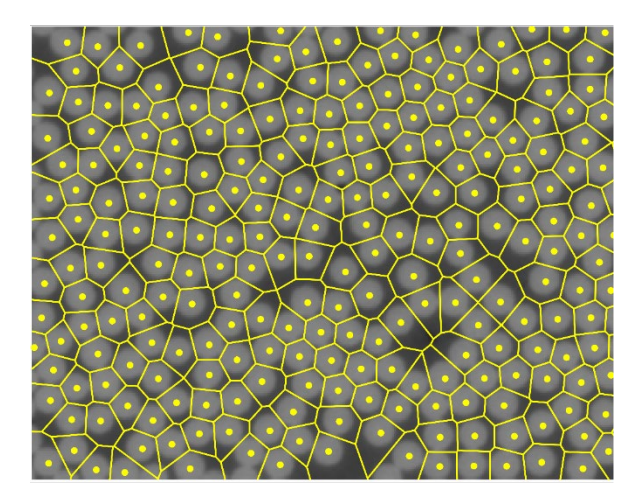


Figure 7. Cropped section of a CT image showing the Voronoi tessellation of the fiber centers

UNIQUE NEIGHBOR CHANGE RATE

The neighbor change rate (ξ_i) is a measure of how often the nearest neighbors of fiber i change along the fiber direction. The neighbor change rate was calculated using the Delaunay triangulation to get each fiber's nearest neighbor in each cross-section. From there the changes in connectivity from section to section were counted for each fiber.

The pixel error in the fiber detection software employed in this study, while virtually insignificant for metrics such as the local volume fraction, lead to oscillations in the nearest neighbor connectivity from cross-section to cross-section (Figure 8). As a result certain fibers contain erroneously high neighbor change counts.

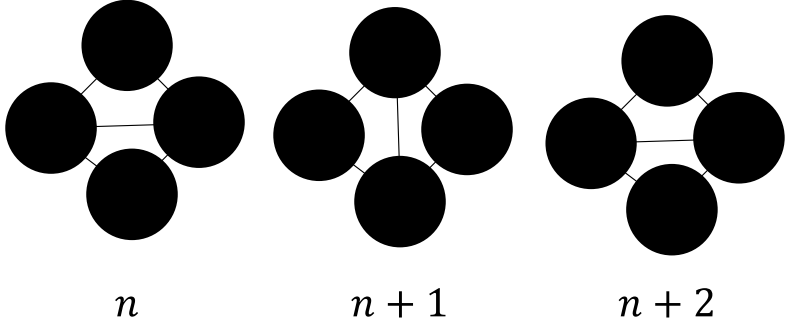


Figure 8. Delaunay triangulation of fibers for successive cross-sections showing oscillating changes in connectivity

To curb this issue the unique neighbor change rate (\dot{X}_i) metric was defined. The UNCR is simply the neighbor change rate where every unique change in nearest

neighbor connectivity is only counted once. That is, once a fiber leaves the connectivity array it cannot return.

In the case of local metrics, it is convenient to compare rates because composite microstructures of different lengths can be compared.

CLUSTERS

The cluster analysis is a method of describing the tendency for groups of fibers to remain together throughout the volume of fiber reinforced composites. In the analysis presented here fiber triads are found using the triangulation of all fiber centers in the first cross-section of an image stack. The cluster analysis used here is presented fully [26]. Due to issues with oscillations of the fiber centers, linearized fibers were used in this analysis. The points along each fiber were recalculated from the parametric equations representing each individual fiber. Alpha shapes of the fibers are used to ensure the boundary fiber connectivity is restricted to the convex hull. The fiber triads found in the first cross-section were held constant for the remainder of the analysis. The cluster metric was defined in terms of the total variation of certain geometric measurements of fiber triads. The total variation of the area, V_A^l , is used here to measure the 3D variation of triad areas within the sample.

$$V_A^l = \sum_{n=2}^N |A^l(x_n) - A^l(x_{n-1})|$$
 (2)

where N is the total number of cross-sections and A^l is the area of triad l at a particular cross-section. It was discovered, however, that it was possible for three fibers to bound a relatively small area but still be spread out. To handle such cases the total variation of the perimeter, V_P^l , was added as a second criterion.

total variation of the perimeter,
$$V_P^l$$
, was added as a second criterion.
$$V_P^l = \sum_{n=2}^{N} |P^l(x_n) - P^l(x_{n-1})| \tag{3}$$

where V_P^l is the total variation of the perimeter, and P^l is the perimeter of triad l at a particular cross-section. The final cluster determination is made using the histogram distributions of both criteria. Otsu's method with three bins was then used to threshold V_A^l and V_P^l independently. In this method, three bins are created, with bin boundaries set such that the variance within each bin is minimized. In the end, the determination of whether a triad is clustered or not depends solely on the triad's relative location in distribution of all triads rather than its specific value and the threshold is invariant of a length scale. The lower thresholds for the area and perimeter variance are then combined in a Boolean operation. For each triad, the values of V_A^l and V_P^l must be below their respective thresholds to be deemed clusters.

The thresholding typically results in a noisy mix of threshold-passing triads, but clusters should be a unique subset of these triads which are aggregated together. To isolate the fiber clusters, a filtering algorithm was created. The intent of the filtering is to remove passed triads not part of a larger cluster, and include fiber triads which are surrounded by a cluster but did not pass the thresholding. This results in a smoothing of fiber clusters, where feature size can be controlled with the filtering method. The basic filtering operation checks whether the neighbors of each triad also passed the thresholding. The algorithm then changes the designation of each triad according to the designation of its neighbors.

A number of cluster metrics have been developed to characterize the shape and size of each cluster, as well as the behavior of the fibers within each cluster. For the purpose of this study 2 metrics have been chosen which describe the shape and size of the clusters in the debulk samples. The first of these metrics is simply the cluster area, which provides info on the size of each cluster in each cross-section.

The second of these metrics is the ratio K, which is calculated from the second moments of area of each cluster. The second moments of area, I_{yy} and I_{zz} , can be calculated for each cross-section (x_n) of a cluster using

calculated for each cross-section
$$(x_n)$$
 of a cluster using
$$I_{ii}(x_n) = \sum_{l=1}^{N_t^m} A^l(x_n) d^l_{ii} \text{ where } i = y, z$$
(4)

where N_t^m is the number of triads in cluster m, $A^l(x_n)$ is the area of triad l at section x_n , and d_{ii}^l is the distance of the cluster centroid to the center of the triads within the cluster in either the y or z directions,. Like the radius of gyration, the moments of inertia are used to understand the geometry of clusters.

The value $K(x_n)$ is used to determine how symmetric the clusters are about both axes, defined as

$$K(x_n) = \sqrt{\frac{I_{yy}(x_n)}{I_{zz}(x_n)}}. (5)$$

When the values for the moments of inertia are very similar, the value of K is close to one, indicating the clusters are fairly symmetric about the y and z axes. When I_{yy} is larger than I_{zz} , it means that the cluster is longer in the z direction than in the y direction, and vice versa. The values for K, therefore, give a sense of how symmetric the clusters are about both axes.

VOIDS

The void content and void distribution of the three samples were computed and contrasted. Voids appear on the grayscale image as regions of low intensity (lower than either the matrix or the fibers) with sharp boundaries. They were identified by thresholding the grayscale image and isolating the connected components of regions formed by pixels of low intensity. It was found necessary to disregard regions with areas less than 10 square microns (i.e. 5 pixels) due to pixilation and salt-and-pepper noise in the image. The center of mass of each remaining void cross-section was computed, and centers on successive layers were joined if their distance did not exceed three microns. This threshold was found to identify cross-sections of the same void, since adjacent distinct voids were separated by tens of microns on average. These computations, as well as voxel-based 3D reconstructions of selected voids, were performed through Wolfram Mathematica.

The presence of superficial contaminations on the sample, discussed above, complicated the reconstruction, since darker spills and discoloration are indistinguishable, purely in terms of grayscale values, from voids (Figure 4). This difficulty was avoided by further restricting attention to those voids that spanned at least two successive cross-sections, since there was no contamination that appeared in the same location on any two successive images. Micro-abrasions and voids whose

major axes are shorter than 5 microns are therefore not included in the volumetric and morphological data.

As regards structural morphology, the CFRP specimens contain three distinct regimes: intra-tow; inter-tow; and regions surrounding stitches. For the purposes of this investigation, attention was focused on voids within the same tow (intra-tow).

The results collected correspond to 2,000 x 5,000 pixel, that is, 1.02mm x 2.55mm image segments from each of the high debulk, low debulk, and benchmark samples, comprising intra-tow regions with no inter-tow interfaces or stitches. The depth of each sample was 199 cross-sections or 500 microns. The void content was found by adding up the total volume of all detected voids and dividing it by the volume of the sample.

RESULTS AND DISCUSSION

Three carbon fiber plates were created from three plies which underwent different levels of debulking. Samples were taken from each plate and imaged using an automated serial sectioning system. Fiber paths and voids were extracted from the images, and various metrics were used to characterize the three different samples. Results of each metric were compared across the three levels of debulking to understand the effect of debulking on the resulting microstructure and void content.

Fiber Metrics

LOCAL VOLUME FRACTION

The local volume fraction is a measure of the area of a fiber to the area of the Voronoi cell it sits in. This formulation of volume fraction can be used to obtain local data for each fiber in every cross-section, and gain insight into the spatial density of the fibers. The histograms for the local volume fraction in each analyzed tow and the global samples are shown in Figure 9. The shapes of the high debulk and low debulk tow histograms are fairly similar in terms of magnitude at the mode and distribution. The benchmark tows, however, have a significantly lower probability density than any of the tows in the other layers. The location of the modes for the benchmark tows occur below 0.6, while the tows of the other layers occur above 0.6 fiber volume fraction. The histograms of the global samples show a similar trend, with the high and low debulk distributions being similar and the benchmark sample being lower at the mode.

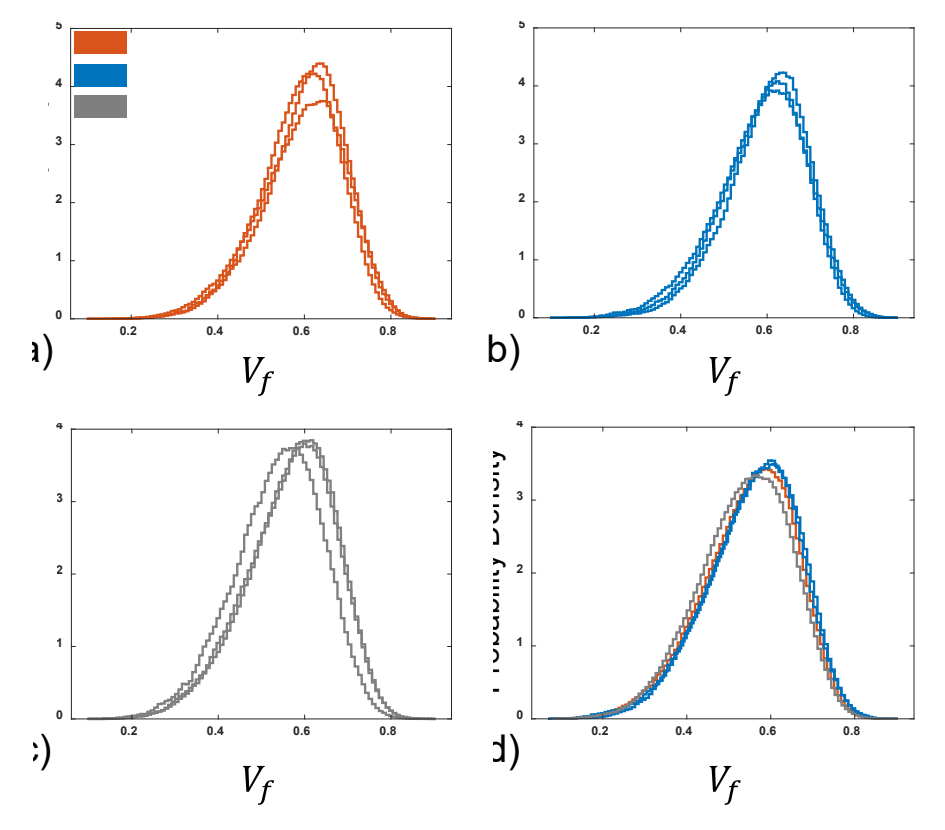


Figure 9. Local volume fraction, V_f , distributions of a) high debulk tows, b) low debulk tows, c) benchmark tows, and d) global samples from each layer

The averages of the three tows analyzed in each layer are shown in Figure 10a, with standard deviations. The average values for the three tows seem to show that the debulking procedure was most effective in the jump from the benchmark sample to the low debulking steps. It can be seen from the standard deviations, however, that each tow contains a lot of overlap in values.

The averages for the global samples in each layer are shown in Figure 10b. Unlike the comparison using tows, the global sample comparison shows that the averages for the high debulk and benchmark layers are both lower than the low debulk layer. The overlap of the standard deviations, however, is greater between the global samples than the tow samples. The magnitudes of the standard deviation are roughly equal in both comparisons.

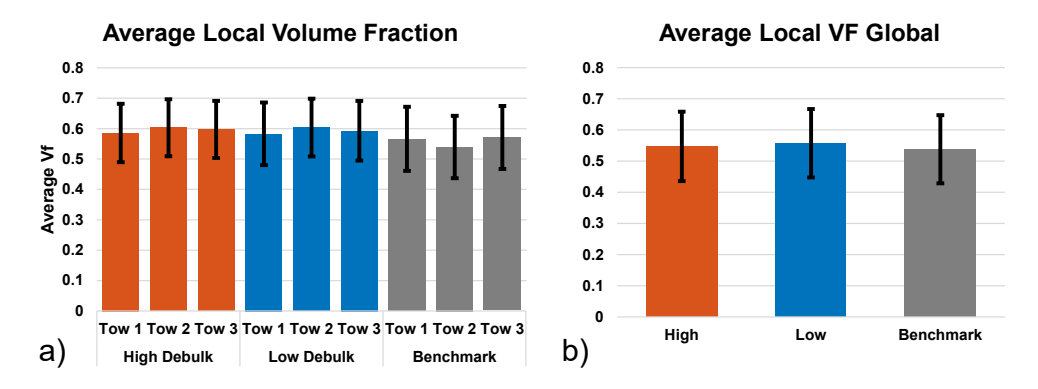


Figure 10. Average local volume fraction values for a) tows in each layer and b) global samples from each layer

The high overlap of the standard deviations suggest that neither the tows, nor the global samples were sufficient in size to truly capture the differences between each layer. Looking at just the averages, there seems to be correlation between the level of debulking and the amount of compaction in the tows. As the number of debulking steps increases, the average volume fraction in each tow seems to also increase. More than three tows per layer are needed to make a final conclusion on this relationship. Additionally, the size of the global sample needs to be increased in future analyses.

UNIQUE NEIGHBOR CHANGE RATE

The unique neighbor change rate metric is a measurement of the amount of meandering that a fiber exhibits, as well as the amount of meandering that occurs around the fiber. Straight fibers surrounded by misaligned fibers may have just as many neighbor changes than misaligned fibers surrounded by straight fibers. The histograms for the unique neighbor change rate in each analyzed tow and the global samples are shown in Figure 11. The distributions are all extremely similar in shape and mode.

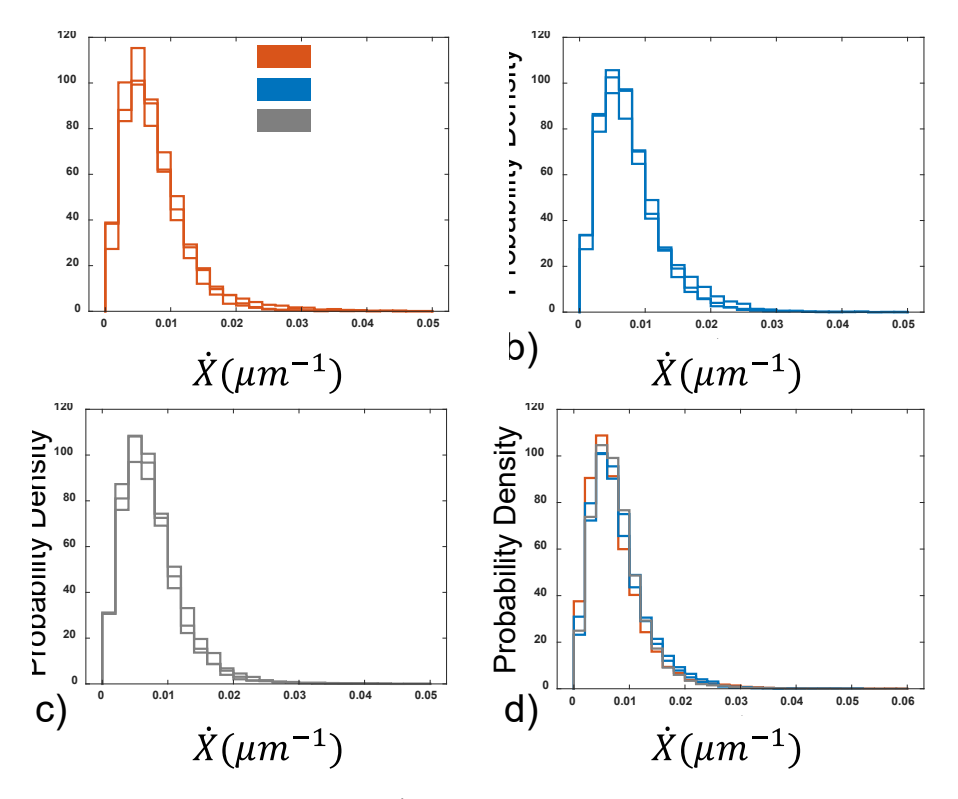


Figure 11. Unique neighbor change rate, \dot{X} , distributions of a) high debulk tows, b) low debulk tows, c) benchmark tows, and d) global samples from each layer

The average values of the unique neighbor change rate for each tow are shown in Figure 12a, with standard deviations. Across each layer the tows seem to show no clear trend in terms of the debulking level versus the number of neighbor changes. The standard deviations for each sample are very large when compared to the averages, and overlap greatly from tow to tow. The results of the global analysis show a very similar story (Figure 12b). The averages for these samples are very close to one another, as well as their standard deviations.

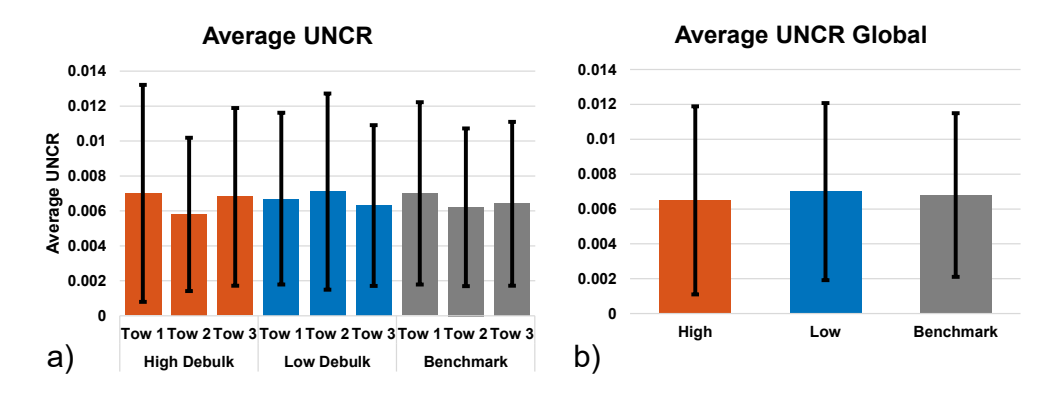


Figure 12. Average unique neighbor change rate values for a) tows in each layer and b) global samples in each layer, with standard deviations shown

The average results coupled with the similarity of the distributions suggest that there is no real correlation between the unique neighbor change rate and the level of debulking applied to the fibers. In other words, the level of debulking may not have an effect on the misalignment of the fibers.

CLUSTER METRICS

The cluster analysis is used to identify bundles of fibers that are oriented together with in a given sample. The results of the cluster analysis for all three tows in the high debulk, low debulk, and benchmark layers are shown in Figure 13. In these plots each cluster is colored differently depending on the order in which the cluster was detected. Looking at the plots of the clusters it can be seen that, in general, the clusters are longer in the direction normal to compaction (y direction).

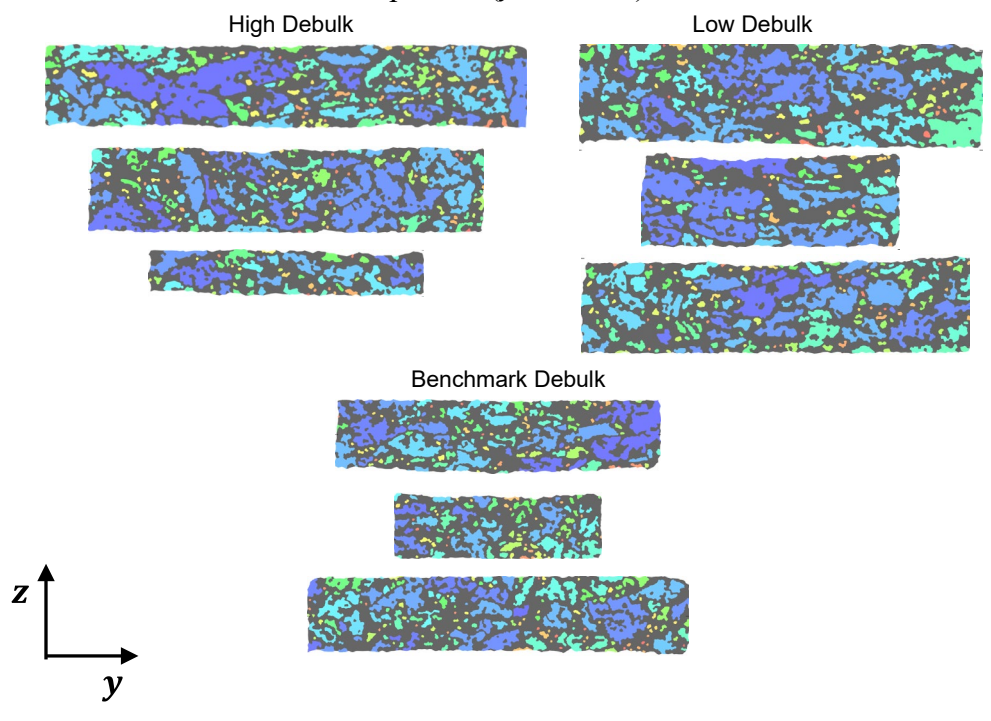


Figure 13. Results of the cluster analysis for all three layers

The histograms for the log of the cluster area and the K ratio are shown in Figure 14. The cluster areas most often occur on the order of 10^2 to $10^3 \,\mu\text{m}^2$ for all tows in all samples. One observation about the area of the clusters is that the larger samples tended to have larger clusters. This makes intuitive sense due to the fact that larger samples simply have more fibers and thus more potential to be part of a cluster. Despite this, the mode of the cluster areas seems to not depend on the size of the sample at all. That is, the most common cluster size range appears constant across both large and small tows.

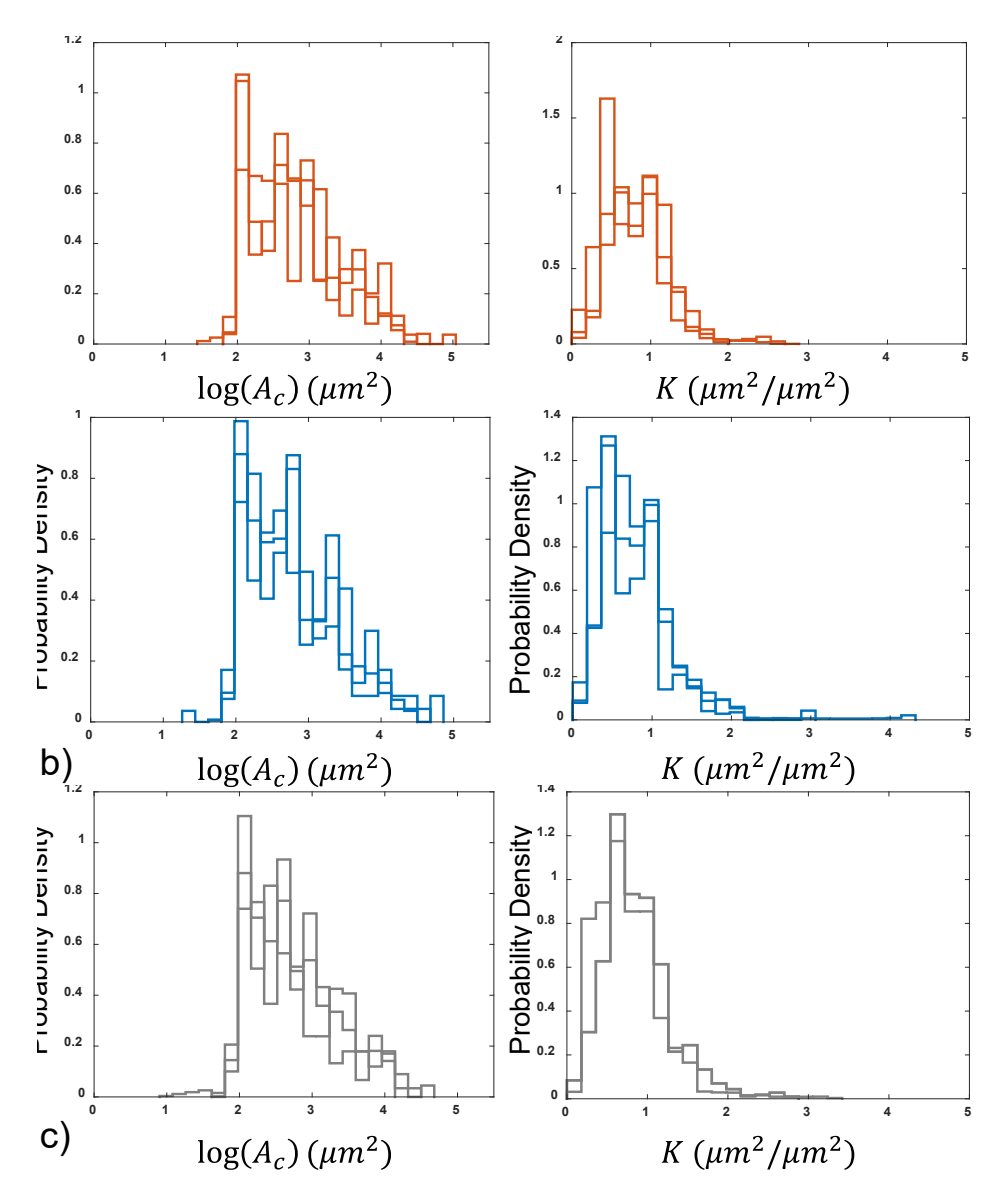


Figure 14. Log of cluster area, A_c , and ratio K for a) high debulk, b) low debulk, and c) benchmark tows

The *K* value is a measure of the symmetry of a cluster about both the *y* and *z* axes. When *K* is below 1 the cluster is longer in the *y* direction, and when *K* is above 1 the cluster is longer in the *z* direction. *K* values near 1 correspond to clusters that are nearly equivalent in their distribution of area about the *y* and *z* axes. The histograms for the *K* ratio show that the majority of clusters in each tow have a *K* value lower than 1. This result shows that the clusters tend to be longer in the *y* direction, which is the direction normal to compaction.

The average values for cluster area are shown in Figure 15a. The results of the average cluster areas show that the clusters in the high and low debulk tows tended to be larger than the clusters in the benchmark sample. The standard deviations were also extremely low for each measurement when compared to the average value. This result suggests that the size of the clusters in each tow could be related to the level of debulking applied. Intuitively, it would make sense that the size of fiber clusters would be larger with the more debulking steps. The increased debulking steps, in theory,

should decrease the distance between neighboring fibers. This decrease in distance would directly affect the variation in area and perimeter for each cluster, causing more fiber triads to pass as clusters.

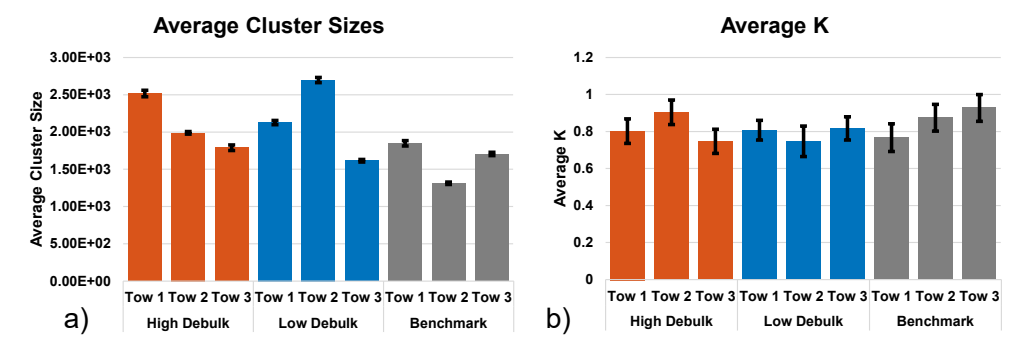


Figure 15. Bar plots of a) average cluster size and b) average **K** value for each tow in each layer, showing standard deviations

The average values for ratio K are shown in Figure 15b. These results confirm what is shown in the histograms of this metric, in which the vast majority of clusters have a K value lower than 1. There is no apparent trend with respect to the level of debulking, besides that fact that all debulked samples have an average below 1, even when the standard deviation is considered. This suggests that the level of debulking is independent of the shape of the fiber clusters within tows.

VOIDS

Voids form within fiber reinforced materials during the resin infusion process. Results of the void analysis are shown in Table 4.

TARIE 2	DECLII TC	OF VOID	ANALYSIS
TADLE Z.	RESULIS		ANALISIS

Layer	# Voids	Max Volume (μm³)x10 ⁴	Min Volume (µm³)	Average Volume (μm³)x10 ⁴	Median Volume (µm³)	Volume STD (μm³)x10 ⁴	Longest Void (μm)	Void Content $\left(\frac{\mu m^3}{\mu m^3 x 10^6}\right)$
High	496	86.9	9.10	1.51	95.6	6.25	442.5	5831.36
Low	301	13.5	7.80	0.521	48.8	1.73	232.5	1236.70
Bench	347	8.93	7.80	0.00541	27.3	0.0087	12.5	14.58

The data clearly affirm the hypothesis that increased debulking increases both the void content and the average void size of CFRPs. Moreover, with increased debulking, the growth in the number of voids, while noticeable, is dwarfed by effect of increased void size. Indeed, the overall increase in void content seems to be entirely due to increases in the mean void volume and the appearance of "gigantic" voids. This can also be seen visually by plotting the centerline plots of the voids for each layer (Figure 16).

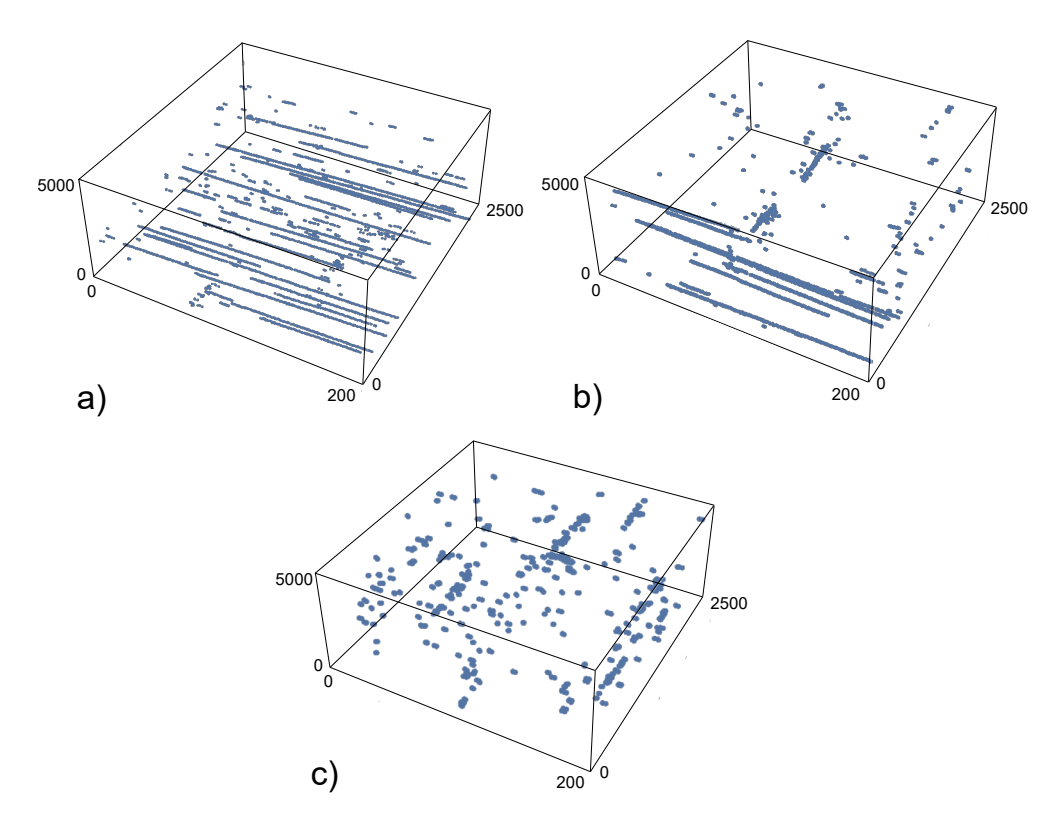


Figure 16. 3D scatter plots of voids in a) high debulk, b) low debulk, and c) benchmark layers

The histogram of logarithms of void volumes suggests that the distribution of void volumes is approximately lognormal around its mode, but there is insufficient data to ascertain the nature of tail distributions and outliers (Figure 17). Microvoids were not included in the statistics due to the difficulty of reliably separating them from image noise, while voids of exceptional length were cut off by one end or the other of the specimens. The 3D reconstruction of these voids suggests that they are macroscopic, perhaps 1mm in full length.

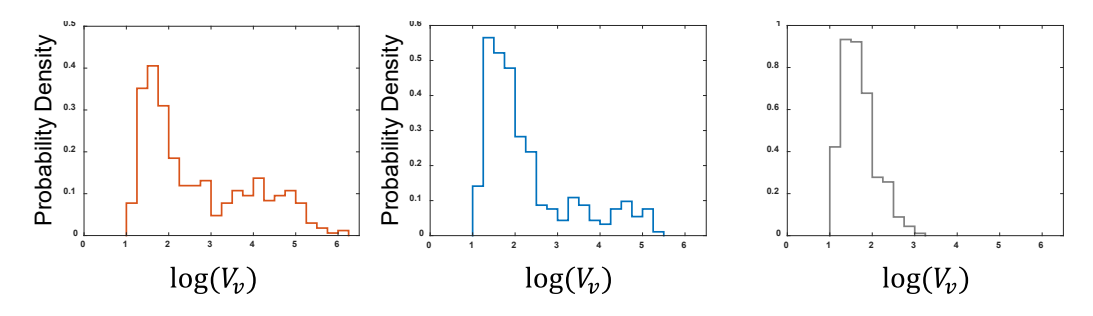


Figure 17. Log of void volume histograms for a) high debulk, b) low debulk, and c) benchmark samples

Voids are approximately prolate spheroids in shape, with major axes parallel to the fiber direction (Figure 18). Unlike those of microvoids, however, the cross-sections of macroscopic voids are clearly not convex. The indentations are due to the presence of nearby fibers. Portraits of voids at their widest cross-sections confirm that they are almost entirely surrounded by a tight perimeter of fibers (Figure 19).

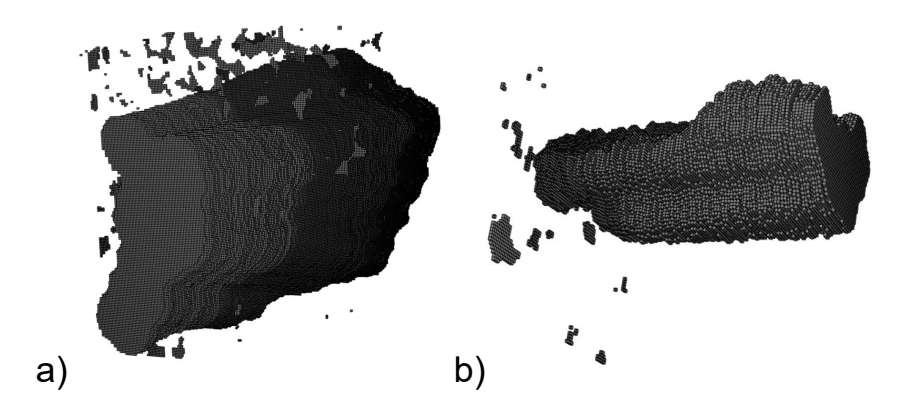


Figure 18. Voxel reconstruction of the largest voids for the a) high debulk and b) low debulk samples

The interface between the voids and nearby matrix-rich areas is negligible, and the diameter of void cross-sections far exceeds the mean spacing between adjacent fibers. It is left for further research to understand the fluid mechanics leading to the formation of these macroscopic voids.

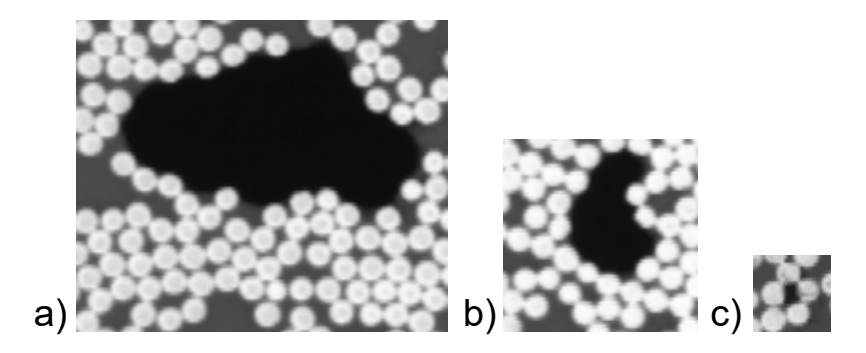


Figure 19. Portraits of maximal void 2D cross-sections for the a) high debulk, b) low debulk, and c) benchmark samples

SUMMARY AND CONCLUSIONS

Debulking is typically done to improve the compaction of carbon fibers prior to infusion, thus improving the performance of cured fiber reinforced composites while avoiding more expensive manufacturing techniques. While work has been done in the past to study the effects of debulking on the void formation within manufactured parts, little has been done in terms of studying the effect on the resulting microstructure. Metrics were developed and employed which permit the study of the special and structural distribution of fibers. Comparison of the local volume fraction distribution showed that the level of debulking seemed to increase the spatial density of carbon fibers in individual tows after just the low debulking steps were performed. In contrast, the results of the global analyses showed no correlation to the level of debulking and the volume fraction. The standard deviations for each global data set overlapped significantly and were large when compared to the average value. This suggests the need for a more random approach to collecting fibers. Selecting random

sections of each layer and analyzing each could shed more light on the true relationship between the level of debulking and the local volume fraction.

The unique neighbor change metric was also used to see if the level of debulking has an effect on the orientation of fibers. The results of this with respect to the tows in each layer showed no clear relationship between unique neighbor change rate and the level of debulking. The average unique neighbor change rate for each tow in the layers where debulking was applied was very similar to the average unique neighbor change rate in the benchmark sample tows. This result was also seen in the comparison between the global samples for each layer. As mentioned previously, the need for more data is highlighted in these results.

The cluster analysis was performed to see whether the level of debulking had any effect on the clusters present within the sample. Clusters were defined as groupings of fibers that remain near each other throughout the length of the sample, independent of orientation. Qualitatively, it can be seen that the clusters present in all samples are longer in the direction normal to compaction. This observation is supported by the results of the *K* ratio metric, which had a mean value less than 1 for all tow and global samples. The cluster areas were also measured and showed one of the clearest trends of any metric. The cluster areas in the high and low debulk tows were higher than the clusters in the benchmark tows. This result makes sense given the way the clusters were generated. Debulking is meant to induce fiber nesting, in which the compaction of fibers is increased and the space between fibers is decreased. This would effectively decrease the volume between fiber triads, thus decreasing the area between triads in each cross-section and clustering more fibers.

Finally, the analysis of voids in all three samples showed that the number and size of voids increased with the level of debulking. The benchmark sample showed the least number of voids and the smallest void volumes, while the high debulk sample showed the largest volumes of all voids. The reconstruction of the voids showed that they are non-convex, and always surrounded by fibers. The surrounding fibers suggest that the presence of the voids is due to the tight packing of the fibers caused by the level of debulking. It is unclear yet whether the voids caused any kind of deviation of the fiber paths. Further analysis needs to be done to see whether the voids present change the orientation of the fibers.

The debulking process is widely used as an alternative to manufacturing methods which compact fibers at a higher cost. Research has shown that the process of debulking can produce favorable volume fractions of fibers, but at the cost of producing voids. The analysis of voids and void content as a function of debulking is an important step in the endeavor to understand the structural effects of debulking itself. Additionally, it is important to understand the resulting microstructure of any manufacturing process. The results presented here are meant to further to effort to understand the effects of debulking on the final strength of a composite part. Identifying the effects of debulking on the resulting microstructure through rigorous analysis and metrics will hopefully bring research a step closer to tailoring manufacturing processes and producing optimal composite parts.

ACKNOWLEDGMENTS

This work is based upon work supported by the National Science Foundation and Air Force Office of Scientific Research under grant number IIP1826232. Any opinions, findings, and conclusions or recommendations expressed in this material are those of the author(s) and do not necessarily reflect the views of the National Science Foundation.

The authors would like to thank Dr. Andy George at Brigham Young University for organizing and performing the debulking experiment, as well as performing the final consolidation of the materials. This work would not be possible if it weren't for his knowledge and input on both the experiment and the subsequent work on voids.

The authors would also like to thank Dr. Evan Pineda and Richard Martin at the NASA Glenn Research center for their funding, time, and assistance with the Robo-MET serial sectioning machine.

REFERENCES

- 1. Williams C, Summerscales J, Grove S (1996) Resin Infusion under Flexible Tooling (RIFT): a review. Composites Part A: Applied Science and Manufacturing 27:517–524. https://doi.org/10.1016/1359-835X(96)00008-5
- 2. de Almeida SFM, Neto Z dos SN (1994) Effect of void content on the strength of composite laminates. Composite Structures 28:139–148. https://doi.org/10.1016/0263-8223(94)90044-2
- 3. Liu L, Zhang B-M, Wang D-F, Wu Z-J (2006) Effects of cure cycles on void content and mechanical properties of composite laminates. Composite Structures 73:303–309. https://doi.org/10.1016/j.compstruct.2005.02.001
- 4. Lambert J, Chambers AR, Sinclair I, Spearing SM (2012) 3D damage characterisation and the role of voids in the fatigue of wind turbine blade materials. Composites Science and Technology 72:337–343. https://doi.org/10.1016/j.compscitech.2011.11.023
- 5. Di Landro L, Montalto A, Bettini P, et al (2017) Detection of Voids in Carbon/Epoxy Laminates and Their Influence on Mechanical Properties. Polymers and Polymer Composites 25:371–380. https://doi.org/10.1177/096739111702500506
- 6. Sisodia S, Bull D, George A, et al (2019) The effects of voids in quasi-static indentation of resin-infused reinforced polymers. Journal of Composite Materials 53:4399–4410. https://doi.org/10.1177/0021998319858024
- 7. Mehdikhani M, Gorbatikh L, Verpoest I, Lomov SV (2019) Voids in fiber-reinforced polymer composites: A review on their formation, characteristics, and effects on mechanical performance. Journal of Composite Materials 53:1579–1669. https://doi.org/10.1177/0021998318772152
- 8. Schell JSU, Deleglise M, Binetruy C, et al (2007) Numerical prediction and experimental characterisation of meso-scale-voids in liquid composite moulding. Composites Part A: Applied Science and Manufacturing 38:2460–2470. https://doi.org/10.1016/j.compositesa.2007.08.005

- 9. Hamidi YK, Aktas L, Altan MC (2005) Effect of packing on void morphology in resin transfer molded E-glass/epoxy composites. Polymer Composites 26:614–627. https://doi.org/10.1002/pc.20132
- 10. Hernández S, Sket F, González C, LLorca J (2013) Optimization of curing cycle in carbon fiber-reinforced laminates: Void distribution and mechanical properties. Composites Science and Technology 85:73–82. https://doi.org/10.1016/j.compscitech.2013.06.005
- 11. Kim YR, McCarthy SP, Fanucci JP (1991) Compressibility and relaxation of fiber reinforcements during composite processing. Polymer Composites 12:13–19. https://doi.org/10.1002/pc.750120104
- 12. Robitaille F, Gauvin R (1999) Compaction of textile reinforcements for composites manufacturing. III: Reorganization of the fiber network. Polymer Composites 20:48–61. https://doi.org/10.1002/pc.10334
- 13. Grieser T, Mitschang P (2017) Investigation of the compaction behavior of carbon fiber NCF for continuous preforming processes. Polymer Composites 38:2609–2625. https://doi.org/10.1002/pc.23854
- 14. Lectez A-S, El Azzouzi K, Binetruy C, et al (2018) Three-dimensional mechanical properties of dry carbon fiber tows subjected to cyclic compressive loading. Journal of Composite Materials 52:2661–2677. https://doi.org/10.1177/0021998317752229
- 15. Pearce N, Summerscales J (1995) The compressibility of a reinforcement fabric. Composites Manufacturing 6:15–21. https://doi.org/10.1016/0956-7143(95)93709-S
- 16. Niggemann C, Song YS, Gillespie JW, Heider D (2008) Experimental Investigation of the Controlled Atmospheric Pressure Resin Infusion (CAPRI) Process. Journal of Composite Materials 42:1049–1061. https://doi.org/10.1177/0021998308090650
- 17. Somashekar AA, Bickerton S, Bhattacharyya D (2007) Exploring the non-elastic compression deformation of dry glass fibre reinforcements. Composites Science and Technology 67:183–200. https://doi.org/10.1016/j.compscitech.2006.07.032
- 18. George A, Hannibal P, Morgan M, et al (2019) Compressibility measurement of composite reinforcements for flow simulation of vacuum infusion. Polymer Composites 40:961–973. https://doi.org/10.1002/pc.24770
- 19. Danzi M, Klunker F, Ermanni P (2017) Experimental validation of through-thickness resin flow model in the consolidation of saturated porous media. Journal of Composite Materials 51:2467–2475. https://doi.org/10.1177/0021998316671574
- 20. Yenilmez B, Caglar B, Sozer EM (2017) Viscoelastic modeling of fiber preform compaction in vacuum infusion process. Journal of Composite Materials 51:4189–4203. https://doi.org/10.1177/0021998317699983
- 21. Matsuzaki R, Seto D, Todoroki A, Mizutani Y (2014) Void formation in geometry–anisotropic woven fabrics in resin transfer molding. Advanced Composite Materials 23:99–114. https://doi.org/10.1080/09243046.2013.832829
- 22. Lundström TS, Gebart BR (1994) Influence from process parameters on void formation in resin transfer molding. Polymer Composites 15:25–33. https://doi.org/10.1002/pc.750150105

- 23. Patel N, Lee LJ (1995) Effects of fiber mat architecture on void formation and removal in liquid composite molding. Polymer Composites 16:386–399. https://doi.org/10.1002/pc.750160507
- 24. Park CH, Woo L (2011) Modeling void formation and unsaturated flow in liquid composite molding processes: a survey and review. Journal of Reinforced Plastics and Composites 30:957–977. https://doi.org/10.1177/0731684411411338
- 25. Staffan Lundström T, Frishfelds V, Jakovics A (2010) Bubble formation and motion in non-crimp fabrics with perturbed bundle geometry. Composites Part A: Applied Science and Manufacturing 41:83–92. https://doi.org/10.1016/j.compositesa.2009.05.012
- 26. Schey MJ, Beke T, Appel L, et al (2021) Identification and Quantification of 3D Fiber Clusters in Fiber-Reinforced Composite Materials. JOM 73:2129–2142. https://doi.org/10.1007/s11837-021-04703-0